

Nanoscale Advances

Accepted Manuscript

This article can be cited before page numbers have been issued, to do this please use: J. I. del Rio, L. Juhász, J. Kalmár, Z. Erdelyi, M. D. Bermejo, A. Martin, I. Smirnova, P. Gurikov and B. Schroeter, *Nanoscale Adv.*, 2023, DOI: 10.1039/D3NA00444A.



This is an Accepted Manuscript, which has been through the Royal Society of Chemistry peer review process and has been accepted for publication.

Accepted Manuscripts are published online shortly after acceptance, before technical editing, formatting and proof reading. Using this free service, authors can make their results available to the community, in citable form, before we publish the edited article. We will replace this Accepted Manuscript with the edited and formatted Advance Article as soon as it is available.

You can find more information about Accepted Manuscripts in the [Information for Authors](#).

Please note that technical editing may introduce minor changes to the text and/or graphics, which may alter content. The journal's standard [Terms & Conditions](#) and the [Ethical guidelines](#) still apply. In no event shall the Royal Society of Chemistry be held responsible for any errors or omissions in this Accepted Manuscript or any consequences arising from the use of any information it contains.

1 **A greener approach to synthesizing metal-decorated carbogels from alginate**
2 **for emerging technologies**

3

4 Juan I. del Río^{a,b}, Laura Juhász^c, József Kalmár^d, Zoltán Erdélyi^c, María D. Bermejo^a, Ángel Martín^a,
5 Irina Smirnova^e, Pavel Gurikov^{f,g}, Baldur Schroeter^{e*}

6

7 ^a BioEcoUva, Bioeconomy Research Institute, PressTech Group, Department of Chemical
8 Engineering and Environmental Technology, Universidad de Valladolid, Prado de La Magdalena S/n,
9 47011 Valladolid, Spain

10 ^b Grupo Procesos Químicos Industriales, Department of Chemical Engineering, Universidad de
11 Antioquia UdeA, Calle 70 No. 52-21, Medellín 050010, Colombia

12 ^c Department of Solid State Physics, University of Debrecen, Egyetem sqr. 1, H-4032 Debrecen,
13 Hungary

14 ^d ELKH-DE Mechanisms of Complex Homogeneous and Heterogeneous Chemical Reactions
15 Research Group, Department of Inorganic and Analytical Chemistry, University of Debrecen,
16 Egyetem tér 1., Debrecen, H-4032 Hungary

17 ^e Institute for Thermal Separation Processes, Hamburg University of Technology, Eißendorfer Straße
18 38, 21073 Hamburg, Germany

19 ^f Laboratory for Development and Modelling of Novel Nanoporous Materials, Hamburg University of
20 Technology, Eißendorfer Straße 38, 21073 Hamburg, Germany

21 ^g aerogel-it GmbH, Albert-Einstein-Str. 1, 49076 Osnabrück, Germany

22

23

24 *Corresponding author Tel.: +49 40 42878 3962

25 E-mail address: baldur.schroeter@tuhh.de

26

27



29 **Abstract**

30

31 In the present work, a series of metal nanoparticle-decorated carbogels (M-DCs) was synthesized
32 starting from beads of parent metal-crosslinked alginate aerogels (M-CAs), comprising Ca(II), Ni(II),
33 Cu(II), Pd(II) and Pt(IV) ions, followed by pyrolysis under N₂ atmosphere up to pyrolysis temperatures
34 of $T_p = 600$ °C. The textural properties of M-CAs are found to depend on the crosslinking ion, yielding
35 fibrous pore networks with high specific mesoporous volume and specific surface area S_v ($S_v \sim 480$
36 $- 687$ m²/g) for M-CAs crosslinked with hard cations, Ca(II), Ni(II) and Cu(II), and comparably loose
37 networks with increased macroporosity and lower specific surface ($S_v \sim 240 - 270$ m²/g) for Pd(II)
38 and Pt(IV) crosslinked aerogels. The pyrolysis of M-CAs resulted in two simultaneously occurring
39 processes: changes of the solid backbone and the growth of metal/metal oxide nanoparticles (NPs).
40 The thermogravimetric analysis (TGA) showed a significant influence of the crosslinking cation on the
41 decomposition mechanism and associated change of textural properties. Backscattered electron
42 scanning electron microscopy imaging (SEM-BSE) and X-ray diffraction revealed that metal ions
43 (molecularly dispersed in the parent aerogels) formed nanoparticles composed of elementary metals
44 and metal oxides in varying ratios over the course of pyrolytic treatment. Increasing the T_p led to in
45 generally larger nanoparticles. The pyrolysis of the nickel-crosslinked aerogel (Ni-CA) preserved to a
46 large extent the mesoporous structure and resulted in the evolution of fine (~ 14 nm) homogeneously
47 dispersed Ni/NiO nanoparticles. Overall, this work presents a green approach for synthesizing metal-
48 nanoparticle containing carbon materials, useful in emerging technologies related to heterogeneous
49 catalysis, electrocatalysis among others.

50 **Keywords:** *green chemistry, aerogels, carbogels, alginate crosslinking, pyrolysis treatment,*
51 *metallic-clusters evolution*

52

53

54

55



56 **Abbreviations**

57

58 M-CA: metal-crosslinked aerogel

59 M-DC: metal nanoparticle-decorated carbogels

60 M: Ca, Ni, Cu, Pd or Pt

61 NPs: Nanoparticles

62



63 Introduction

64

65 Since the discovery of aerogels in the 1930s, a special attention has been paid to their development
66 for a number of industrial applications.^{1,2} Given their nanoporous, thermal and electrical properties,
67 breakthroughs in the past decades have been made in the sector of foods, biomedical, wastewater
68 treatment, pollution, construction, electrode materials and catalysis.^{3,4} Since the late 1980s carbon
69 aerogels (carbogels) have presented a promising alternative for natural carbonaceous materials, due
70 to the possibility of controlling porosity, purity and mechanical strength by adjustments of the
71 synthesis pathway.⁵ The tailorable textural and structural features of carbogels allow us to overcome
72 some constraints related to metal-nanoparticles materials, such as formation of metal-species
73 aggregates, pore blocking and leaching. Other features such as large specific area, low density, low
74 thermal and high electrical conductivity as well as hydrophobicity make them attractive materials as
75 catalyst supports, chemical adsorbents and energy storage as capacitors.⁶ The polycondensation of
76 resorcinol with formaldehyde under alkaline conditions was a typical pathway to obtain carbogels in
77 recent decades. Other synthetic polymers, such as polybenzoxazines, polyureas, polyimides,
78 polyamides and polyurethanes, have also been used as porous precursors for carbogels.⁷ For
79 instance, Raptopoulos *et al.* produced carbogels from polyurea crosslinked alginate, with an
80 increased carbonization yield of up to 37%, which in turn improves surface functionalities (e.g.
81 electrical conductivity and catalytic activity) of the carbogel by contributing with oxygen and nitrogen
82 functional groups.⁸ Recently, Zhang *et al.* developed a series of carbon aerogel-based
83 electrocatalysts with transition metal-nitrogen sites for the electroreduction of CO₂.⁹ The starting
84 hydrogel was formed *via* complexation between 2,2'-bipyridine-4,4'-dicarboxylic acid and selected
85 metal ions (Ni, Fe, Co, Mn and Cu) followed by physical crosslinking by polypyrrole. Baumann *et al.*
86 incorporated copper in a carbogel matrix from formaldehyde polymerization, achieving a uniform
87 dispersion of spherical metal nanoparticles, ranging from 10 to 50 nm.¹⁰ In another study, potassium-
88 doped hydrogels were synthesized via formaldehyde polymerization with the potassium salt of 2,4-
89 dihydroxybenzoic acid: These hydrogels were formed on monodisperse polystyrene particle



90 templates (diameter = 300 or 450 nm). Subsequent ion exchange with Ni, Co or Cu-salts and
91 supercritical drying followed by pyrolysis at 800 °C then led to macroporous ordered carbons.¹¹ The
92 materials obtained presented dense networks of interconnected carbon particles with hierarchical
93 pore structure of meso- and microporosity in the wall that facilitates the accessibility to the metal sites.
94 In the conventional synthesis of metal-containing carbonaceous 3D structures, the incorporation of
95 metals requires subsequent post-functionalization, leading to the need for additional process steps
96 and resource consumption. As an example, a sulphonated starch-based support, is first pyrolysed at
97 400 °C and subsequently impregnated with palladium acetate (10% by weight) in acetone.¹² Wet
98 impregnation, along with other elaborate methods, e.g., chemical vapor deposition¹³ represent
99 additional challenges such as: i) post-distributing metal clusters homogeneously through the
100 adhesive-resistant carbon network, and ii) aggregation of dispersed metals on the carbon surface
101 resulting in the formation of large metal cluster. Despite the remarkable properties exhibited by
102 materials generated via the aforementioned methods, they rely on expensive chemicals and have
103 adverse environmental impacts. Consequently, there has been a growing interest in exploring
104 alternative carbon sources, particularly non-expensive and abundant polysaccharides. Especially
105 polysaccharides derived from species with a large capability to fix carbon dioxide, such as the brown
106 algae, have gained much interest as precursors for the synthesis of nanoporous carbon materials.^{14,15}
107 From a sustainable perspective, this CO₂ capture feature can add value to novel algae-derived
108 nanomaterials. On average, brown algae species contains ~ 40 % alginate, an anionic biopolymer
109 that can be easily crosslinked with cations for the preparation of hydrogels.^{16,17} For example, Meng
110 *et al.* crosslinked sodium alginate with CaCl₂ to obtain a gel that was dried at 50 °C for 3 h, and
111 pyrolyzed at temperatures up to 1000 °C, under nitrogen atmosphere.¹⁸ The resulting carbon aerogel
112 was soaked in 2M of HCl and washed with deionized water to obtain a near neutral sample. In the
113 synthesis of cellulose-based carbogels for the removal of heavy metals from wastewater, Alatalo *et*
114 *al.* employed concentrated sulfuric acid to catalyze the degradation of cellulose prior to hydrothermal
115 carbonization.¹⁹



116 The above reports evidence the need for consolidating the production of carbogels based on
117 inexpensive and more abundant biomass-derived carbon sources, while minimizing the use of no-
118 green chemicals during the process. On the basis of the principles of green chemistry and modern
119 aerogel science, the present work aims at developing an easy, flexible, and inexpensive strategy
120 towards green and sustainable metal-decorated carbogels. The selection of alginate as the carbon
121 source allowed the reduction of production costs and carbon footprint. Therefore, a series of metal
122 nanoparticle-decorated carbogels (M-DCs) were synthesized, starting from the beads of parent
123 metal-crosslinked aerogels (M-CAs), comprising the ions Ni(II), Cu(II), Pd(II), Pt(IV). Because Ca(II)
124 is the most commonly used ion for alginate crosslinking and in the alginate aerogel production, Ca-
125 crosslinked gels were included in the study as a reference material. The *in situ* generation of
126 monodispersed metal-nanoparticles was controlled by the pyrolysis temperature, with no additional
127 post-modification step. The conversion of the biopolymer-aerogel network into the corresponding
128 carbogels was studied with a focus on the changes in textural characteristics during the transition and
129 the evolution of the metallic clusters in the range of low pyrolysis temperatures < 600 °C.

130

131 **Materials and methods**

132

133 *Chemicals*

134

135 The fine powder of sodium alginate Hydagen 500, was used as received from BASF (Ludwigshafen,
136 Germany). The metal precursors were: calcium chloride dihydrate ($\text{CaCl}_2 \cdot 2\text{H}_2\text{O}$) (>99%, Carl Roth
137 catalog number: T885.3), nickel (II) nitrate hexahydrate (>99%, Bernd Kraft, catalog number: 15306),
138 copper (II) sulfate pentahydrate (>99%, Riedel-de Haën), palladium (II) nitrate dihydrate (~40% Pd
139 basis; Sigma Aldrich, catalog number: 76070-1G) and platinum (IV) chloride (assay 96%; Sigma
140 Aldrich, catalog number: 206113-1G). All chemicals were used without further purification.

141 *Synthesis of metal-crosslinked aerogels (M-CAs)*

142



143 A 2 wt% aqueous solution of alginate was prepared by adding sodium alginate powder to
144 demineralized water. The solution was first stirred for 10 min at 500 rpm and then stirred at 1000 rpm
145 up to 2 h at room temperature. Before further usage, the solution was stored at room temperature for
146 12 h to allow the solution to settle. Hydrogel particles were prepared by adding 35 g of alginate
147 solution to a dripping device (**Fig. S1**) that consisted of a separating funnel connected to a
148 compressed air supply and equipped with a nozzle made from a micropipette tip (10 mL) and a custom
149 cut syringe needle (0.6 mm ID and 3 mm length). The falling distance (approx. 7 cm from the gelation
150 bath) and compressed air pressure (< 0.5 bar) were kept constant throughout all experiments. Nickel,
151 copper, palladium, platinum and calcium containing aerogels were prepared by dripping the alginate
152 solution in an aqueous gelation bath with a corresponding salt, where droplets quickly formed
153 hydrogels when coming into contact with a gently stirred gelation salt solution. Three different
154 concentrations c_m of Ca(II), Ni(II) and Cu(II) metal salts were set in the gelation bath ($c_m = 17, 180$
155 and 380 mmol/L), Pd(II) and Pt (IV) salts were used at a constant c_m (17 mmol/L). After a gelation
156 time of 20 min, the gels were separated from the gelation solution, washed twice with demineralized
157 water and several times with ethanol (99.8%) until a final ethanol concentration ≥ 96 wt% was
158 achieved. According to the previous works the Pd(II)-crosslinked gels showed a color change to
159 orange-brown when soaked in ethanol. This was attributed to the reduction of a portion of Pd(II).²⁰
160 However, this phenomenon was proved to have no effect on the formation or on the final structure
161 of the gel. The alcogels were sealed in filter bags and transferred into a high-pressure vessel (3.9 L) for
162 supercritical drying (70 °C, 120 bar) under a constant CO₂ flow (120 g/min) for 6 h. The dried M-CA
163 beads were collected after slow depressurization (1 bar/min) and stored in a desiccator for further
164 analysis and pyrolysis.

165

166 *Preparation of metal nanoparticle-decorated carbogels (M-DCs) and thermogravimetric analysis*

167

168 Thermogravimetric analysis (TGA) of M-CAs and carbogel preparation were carried out
169 simultaneously in the same TGA equipment (Linseis STA-PT1600) under a flow of 100 cm³/min of



170 nitrogen. The samples were heated up to 90 °C at a heating rate of 5 °C/min, followed by a dwelling
171 phase of 45 min. Subsequently, the temperature was raised to the desired final temperature at a
172 heating rate of 5 °C/min, followed by an additional dwelling time of 60 min. Six different final pyrolysis
173 temperatures T_p (150, 285, 380, 450, 525 and 600 °C) were set as part of the thermal stability analysis
174 and M-DC production. For both Pd and Pt containing gels, temperatures of 265 °C and 365 °C were
175 applied instead of 285 °C and 380 °C, respectively. Between 17 mg and 161 mg of each sample was
176 used, depending on the T_p .

177

178 *Characterization of M-CAs and M-CDs*

179

180 The metal content was determined via ICP-OES using a Perkin Elmer Optima 8300 DV. Samples
181 were previously dissolved in a combination of HNO₃, HCl and HF solution. The textural properties of
182 M-CAs and M-DCs were analyzed by N₂ adsorption-desorption measurements (Nova 3000e Surface
183 Area Analyzer Quantachrome Instruments, Boynton Beach, FL, USA). An overall sample mass of
184 20–30 mg was used and all samples were degassed under vacuum at 60 °C for at least 6 h prior to
185 each analysis. The Brunauer-Emmett-Teller (BET) method was used to estimate the specific surface
186 area (S_V), the pore volume of the mesopores (V_{meso}) and pore diameter (d_{meso}) were determined by
187 the Barrett-Joyner-Halendia (BJH) method. All gas sorption experiments were carried out as single
188 determinations with an estimated relative measurement error of 5%. The particle size and sphericity
189 SPH of M-CA beads were determined using a Camsizer XT system (Retsch Technology) in free fall
190 mode according to our previous works.²¹ Skeletal densities ρ_s were determined via helium pycnometry
191 (Multivolume Micromeritics 1305, 4-fold determination). The bulk densities were calculated from the
192 weight of beads that filled a graduated cylinder (volume = 0.35 cm³). The total porosity ε was
193 estimated based on former work²², as follows:

$$194 \quad \varepsilon = (1 - \rho_b / \rho_s) \cdot 100\%$$

195 where ρ_b is the bulk density, and ρ_s is the skeletal density.



196 The outerskin and inner pore structure morphologies of the M-CAs were characterized by scanning
197 electron microscopy (SEM, Zeiss Supra VP55, Jena, Germany). The measurements were carried out
198 under high vacuum at an accelerating voltage of 3 – 5 kV.

199 Reducibility and oxidizability of Pd-CA and M-DCs were determined by means of temperature
200 programmed reduction (H₂-TPR). In a pretreatment step, the sample was heated at a rate of
201 10 °C/min to 150 °C, maintained for 0.5 h under a constant flow (50 cm³/min) of pure argon and finally
202 returned to room temperature to start the data collecting. The H₂-TPR experiments were conducted
203 up to temperatures of 1000 °C under a constant flow of H₂/Ar (10% v/v; 50 cm³/min) at a heating rate
204 of 10 °C/min, in a Autochem II 2920 Micromeritics equipment, coupled to a quadrupole mass
205 spectrometer (Pfeiffer-Vacuum Modelo Omnistar). Hydrogen consumption was monitored by the
206 thermal conductivity detector. Before the detector, an ice trap was used to retain any water formed
207 during the reduction.

208

209 *Characterization of M-DCs via backscattered electron imaging and X-ray diffraction*

210 In order to image the metallic nanoparticles (NPs) in M-DCs obtained at different pyrolysis
211 temperatures, low voltage scanning electron microscopy was performed using a ThermoFisher
212 Scientific Scios 2 microscope. Backscattered electrons (BSE) were detected. BSE electrons are from
213 a deeper interaction volume of the incident beam. The intensity of BSE shows a significant
214 dependence on the atomic number, which results in a contrast between the elements in the BSE
215 images. The contrast correlates with atomic number: brighter regions correspond to higher atomic
216 numbers. The electron beam resolution was 1.6 nm at the optimum working distance < 5 mm at 2 kV
217 accelerating voltage. The samples were fixed with a vacuum-resistant carbon tape on the sample
218 holder. Sputter coating was not applied in this case because even a 5 nm thick sputtered gold layer
219 can dramatically alter the morphology and the surface structure of the aerogel.²³

220 X-ray diffraction patterns of M-DCs samples were collected under Cu-K α 1 radiation (Cu-
221 K α 1 = 0.154059 nm) using a Rigaku SmartLab 9 kW X-ray diffractometer (XRD) with the following
222 measurement conditions: measurements were carried out in Bragg-Brentano ($\Theta/2\Theta$) mode, between



223 35 and 80° using a scan rate of 5°/min. The average crystallite size for each component of the NPs
224 was calculated from the XRD data. Quantitative analysis of the XRD pattern was carried out using
225 Rietveld refinement using the SmartStudio II software. In this process, the measured XRD profile is
226 approximated by a calculated one that includes all instrumental and structural parameters. This
227 method applies a non-linear least squares method based on a wide range of free parameters such
228 as unit cell dimension, crystal structure, and peak shape. Using this fitted graph, quantitative
229 information can be deduced from the XRD pattern.

230

231 RESULTS AND DISCUSSION

232 *Properties of metal ion crosslinked aerogels (M-CAs)*

233 The dripping method using bivalent metal ions resulted in immediate gelation with the formation of
234 hydrogel beads when the solution droplets hit the gelation bath. When converted into aerogels, the
235 beads showed unimodal size distributions with an average particle mean diameter of 1.41 ± 0.06 μm
236 and sphericities in the range of SPH = 0.82 – 0.91 (**Fig. S2 – S3**). In contrast to gelation via bivalent
237 ions, the use of Pt(IV) as a crosslinker led to formation of weak wet gels of an undefined shape during
238 gelation and final dry aerogels of foam-like character (**Fig. S3 e**). These observations are in line with
239 previous works, which showed that the crosslinking of alginate with metals strongly depends on the
240 hard-soft character of the ions.²⁴ The low capability of Pt(IV) to crosslink alginate chains may be
241 attributed to the softer character of the ion as compared to the other crosslinking metal ions in this
242 work, which are well coordinated by hard oxygen atoms in negatively charged carboxylate groups
243 and –OH-groups of β -D-mannurate (M) and of α -L-gulonate (G) building blocks. Additionally, Pt(II)
244 as well as Pt(IV) tend to form characteristically inert “inner-orbital” type complexes in general²⁵:
245 therefore, the reaction rates of complex formation change significantly with the type of the original
246 ligand, as well as with additional factors, such as pH. In our case, we can conclude that either 1) the
247 coordination of Pt-ions in the alginate matrix was not strong enough or 2) the ligand exchange with
248 hydrated PtCl_4 was not fast enough to fix the shape of the alginate solution during gelation before it
249 is dispersed. These effects are also indicated by the results of the ICP-OES analysis, which yielded



250 by far the smallest metal mass with respect to the alginate mass (r_{metal}) in the Pt-containing aerogel
 251 (**Table 1**). The low r_{metal} value for Pt(IV) may result from either low affinity of Pt(IV) to the alginate
 252 matrix or washing out effects during the washing/solvent exchange steps as a result of weak
 253 coordination. Coordination of other metal ions resulted in a significant increase in r_{metal} . Aerogel
 254 skeletal density correlates with the ratio of r_{metal} and parent metal density (**Fig. S4, left**) (with exception
 255 of Ca-CA, since calcium-chloride and alginate show relatively similar parent densities). While no
 256 systematic relation between r_{metal} and textural properties was determined, the type of crosslinking ion
 257 has a strong effect on the overall mesopore volumes and specific surface areas. Gelation via
 258 comparably hard ions Ca(II), Ni(II) and Cu(II) resulted in higher specific surface areas as well as
 259 mesopore volumes as compared to Pd(II) and Pt(IV) crosslinked gel, whereas the trend of the specific
 260 surface area is in line with the affinity of different bivalent ions with alginate molecules.^[26] Hereby,
 261 values of S_v (480 – 687 m²/g) are in the typical range as reported for Ca(II), Cu(II) and Zn(II)
 262 crosslinked alginate and alginate-polyurea hybrid aerogels.^{8,20,24, 27,28}

263 **Table 1** Properties of M-CAs crosslinked with different metal ions at constant $c_m = 17$ mmol/L.

Material [-]	r_{metal} (wt%)	S_v (m ² /g)	d_{meso} (nm)	V_{meso} (cm ³ /g)	ρ_s (g/cm ³)	ρ_b (mg/cm ³)	Total porosity (%)
Ca-CA	8.9 ± 0.5	494 ± 25	41.6	7.0 ± 0.4	1.71 ± 0.09	90.5 ± 0.3	94.7
Ni-CA	9.5 ± 0.2	480 ± 24	41.4	6.5 ± 0.3	1.9 ± 0.2	35.8 ± 0.2	98.1
Cu-CA	11.1 ± 0.2	687 ± 34	17.4	6.7 ± 0.3	2.3 ± 0.1	106.8 ± 0.1	95.1
Pd-CA	12.9 ± 0.6	243 ± 12	17.0	2.3 ± 0.1	4.6 ± 0.9	85.68 ± 0.04	98.1
Pt-CA	3.40 ± 0.04	268 ± 13	27.1	1.29 ± 0.01	1.69 ± 0.07	-	-

264

265 To the best of our knowledge, this work is the first example of purely Pt(IV) crosslinked alginate
 266 aerogels. We also determined a considerably higher specific surface area for Pd-CA (242 m²/g) than
 267 reported elsewhere (52 m²/g).²⁰ The low surface areas in the compared work could result from the
 268 presence of excess free metal salt in the alginate matrix (as also indicated by the high Pd content
 269 used of r_{metal} 17.6 wt%), which would lead to a decrease in S_v given the large difference in atomic

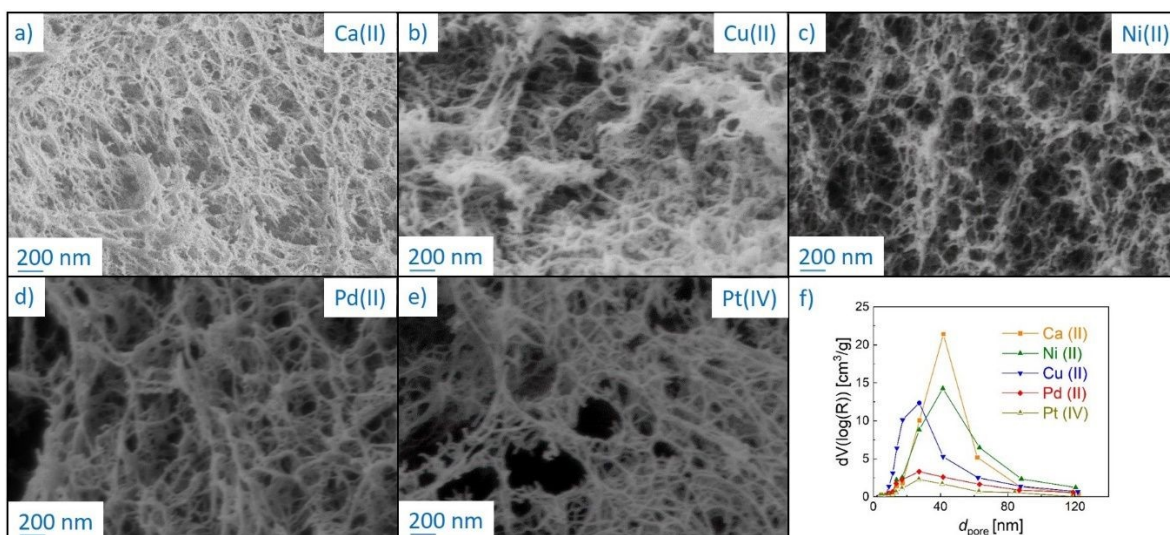


270 mass of the metal compounds as compared to carbon. In this work, the decrease in S_V was also
271 obtained, when increasing the metal salt concentrations of Ca(II), Ni(II) and Cu(II)-salts in the gelation
272 bath above $c_m = 17 \text{ mmol L}^{-1}$ (**Fig. S4, right**) as well as in the work of Miller *et al.*, who obtained a
273 decreased S_V with increasing metal loading in the Ru/carbogel nanocomposite.²⁹ In contrast to the
274 trend of the specific surface area, no significant differences were found in the pore size distributions
275 and mean pore diameters if c_m is increased above 17 mmol/L (**Fig. S5**). This shows that additional
276 ions in the gelation bath do not additionally contribute to crosslinking and cause no microstructural
277 changes.

278 Since no metal salt crystals or deposits were detected in SEM analysis in any substrates (**Fig. S6 -**
279 **S10**) produced at $c_m = 17 \text{ mmol/L}$, we conclude that metal ions were quantitatively integrated into the
280 alginate matrix at the given concentration. Typical macro- to mesoporous ($d_{\text{pore}} = 5 - 50 \text{ nm}$) fibrous
281 microstructures are visible in the SEM pictures, with relatively broad meso pore size distributions and
282 mean mesopore diameters d_{meso} being in the range of 17 – 42 nm (**Fig. 1**). Optical evaluation of SEM
283 pictures shows, that crosslinking with Pd(II) and Pt(IV) yields comparatively loose networks with a
284 significant fraction of macropores, whereas the Cu(II) crosslinked gel shows the densest network with
285 less visible pores in the macroporous range (**Fig. 1 a) - e**), **Fig. S6 - S8**). The qualitative results from
286 SEM are in line with results from gas sorption analysis, which yielded lower mesopore volumes for
287 Pd(II)-CA and Pt(IV)-CA.

288





289

290 **Fig. 1** a) – e) SEM pictures of inner pore structures of M-CAs crosslinked with different metal ions at $c_m =$
 291 17 mmol/L and f) their pore size distributions. Lines are drawn to guide the eye.

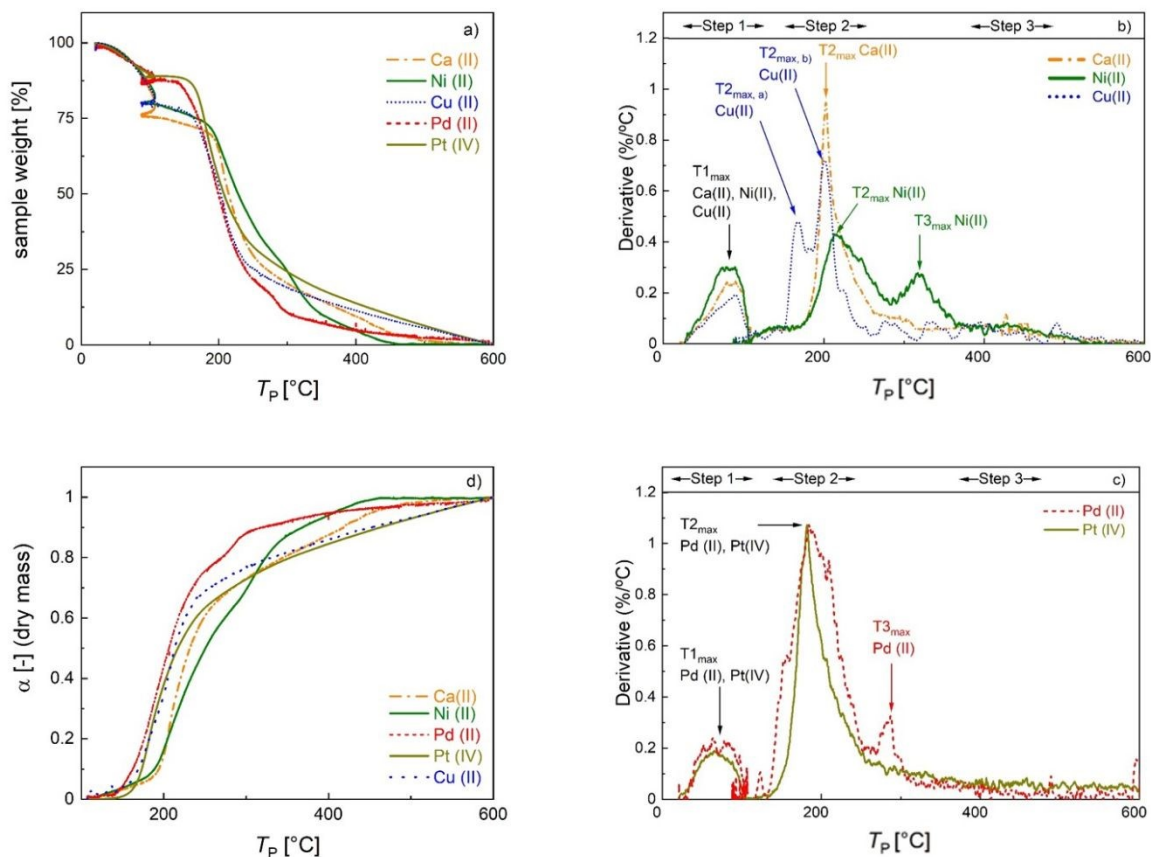
292 Furthermore, a thin denser but still porous outer layer is identified in SEM pictures of aerogels beads
 293 (**Fig. S9 - S10**). This result is in line with previous works, and it is caused by the gelation mechanism.
 294 When sol droplets hit the gelation bath, the immediate complexation of alginate by metal ions on the
 295 surface of droplets leads to formation of a comparably dense, porous skin, followed by a slower,
 296 diffusion controlled completion of the reaction in the inner droplet part.⁸ In summary, the
 297 microstructure of M-CAs is determined by the metal ion chosen for the crosslinking of alginate, while
 298 keeping the total porosity at a constant level. In the next step, the pyrolysis of the produced M-CAs
 299 was investigated for gels produced at $c_m = 17$ mmol/L.

300 *Influence of pyrolytic treatment on mass loss and textural properties*

301 Thermogravimetric analysis (**Fig. 2, a**), and derivative thermogravimetric (DTG, **Fig. 2, b-c**) curves
 302 were recorded to investigate the mass loss of M-CAs during pyrolysis in the whole temperature range
 303 up to final pyrolysis temperatures of $T_p = 600$ °C at a constant heat rate and to identify T_p values, at
 304 which the most significant changes occur. Signals in the DTG curves represent major mass loss and
 305 are used to determine the thermal behavior steps of the materials³⁰, whereas the individual peaks
 306 and maxima are defined in order of appearance as peak X and TX_{max} (with $X = 1 - 3$). The



307 decomposition patterns of all samples can generally be divided into three distinct main steps: 1)
308 moisture loss; 2) biopolymer degradation and 3) slow sustained degradation.³¹



309

310 **Fig. 2** Normalized TGA curves a), DTG curves b), c) and degree of conversion profiles d) of M-CAs crosslinked
311 with different metal ions. See text for details.

312 Alginate aerogels crosslinked with different metal ions show a metal-specific decomposition profile
313 (**Table 2**). The first DTG peak ($T_P = 22 - 108$ °C) is due to moisture loss. A relatively high mass loss
314 (6 - 18 % with respect to the initial mass of the sample, denoted as Δm_{water} in **Table 2**) is rather
315 expected at this stage given the hydrophilic and porous nature of the materials. The second DTG
316 peak occurs in the range 130 – 255 °C for Ca-, Cu- and Pt-CAs and 130 – 364 °C for Ni- and Pd-
317 CAs. The second peak corresponds to the major mass loss of 39 - 61% (denoted as Δm_d and
318 calculated with respect to the dry mass, i.e. the mass after the first step). The onset temperature T_{onset}
319 of peak 2 is assumed to mark the beginning of the thermal scission of the carboxylate/carboxylic acid



320 groups via decarboxylation/decarbonylation and was determined to follow the order: Pd(II) \approx Pt(IV) <
 321 Cu(II) < Ca(II) \approx Ni(II). In general, the decomposition mechanism of metal-crosslinked alginates is
 322 complex and far from being completely understood. For instance, over 20 different degradation
 323 products were determined in the decomposition of Ni- and Cu-crosslinked alginate in each case,
 324 suggesting metal-specific decomposition mechanisms.^{32,33}

325 **Table 2** Thermal parameters in the pyrolysis of different M-CAs.

Material [-]	DTG-peak 1 [°C]	DTG-peak 2 [°C]	DTG-peak 3 [°C]	T _{1max} [°C]	T _{2max} [°C]	T _{3max} [°C]	Δm_{water} peak1 [%]	Δm_{d} peak2 [%]	Δm_{d} peak3 [%]	Δm_{d} total [%]
Ca-CA	27 - 108	174 - 255	-	65	185	-	17.7	39.2	-	67.9
Ni-CA	22 - 108	174 - 283	283 - 365	79	215	318	17.1	46.0	21.8	81.3
Cu-CA	22 - 108	150 - 255	-	87	162 ^{a)} 202 ^{b)}	-	13.1	44.2	-	67.4
Pd-CA	22 - 107	131 - 255	267 - 309	68	186	285	12.2	41.6	5.7	54.5
Pt-CA	22 - 107	135 - 255	-	65	182	-	10.2	60.9	-	95.3

326 a), b): see assignment in Fig. 2.

327 The decomposition profiles observed for Ca(II)-, Cu(II)-, and Ni(II) are consistent with previous works,
 328 whereas the T_{onset} of Ni(II)-crosslinked alginate is shifted to higher temperatures.^{8,33} Differences in the
 329 values of T_{onset} and $T_{2\text{max}}$ compared to the cited works may be attributed to the alginate composition
 330 (G/M ratio, molecular weight) as well as to the different degree of crosslinking.³³ For the Cu(II)-
 331 crosslinked sample, a DTG duplet peak is recorded at 165 and 203 °C, which was also observed in
 332 other works.^{8,31} In the decomposition of pure metal salts, the duplet peak at lower temperatures (45 -
 333 58 °C) corresponds to the formation of trihydrate and monohydrate species of the pentahydrate
 334 sulfate.^{34,35} However, in this work this phenomenon took place at higher temperature, suggesting a
 335 strong interaction of the Cu-complex with alginate chains. In contrast to strong coordinating ions, T_{onset}
 336 for alginate crosslinked with soft Pd(II) and Pt(IV) ions is shifted to lower temperatures. Furthermore,
 337 a third peak appeared at $T_{\text{p}} > 265$ °C for Ni(II)- and Pd(II)-crosslinked samples may be ascribed to
 338 the decomposition of the remaining metal precursor or to the further decomposition of alginate. In the



339 case of Ni-CA, a relatively high mass loss ($\Delta m_d > 20\%$) in this region points out rather biopolymer
340 decomposition.^{36,37}

341 The overall mass loss with respect to the dry mass (“ Δm_d , total” in **Table 2**) covers a wide range (55–
342 95 %). Literature results for ionic crosslinked alginate aerogels are close to the upper values of this
343 range.^{8,38} In our case, the variation in the total mass loss is linearly related to r_{metal} (**Fig. S11**), showing
344 that the variations in overall yield can be attributed to the amount of non-pyrolyzed inorganic material.
345 Due to significant differences in the total mass loss caused by variation of inorganic/organic
346 component ratios, additional insight into effect of individual metal ions on biopolymer decomposition
347 is provided by plotting the degree of conversion α against T_P (**Fig. 2, d**), which is defined as:

$$348 \quad \alpha = \frac{m_{0,d} - m_n}{m_{0,d} - m_{\text{end}}}$$

349 with m_0 is the initial dry mass after completion of the drying step ($T_P = 107 - 108$ °C), m_n is the mass
350 at the corresponding temperature $T_{P,n}$, and m_{end} is the final sample mass at 600 °C.^[31]

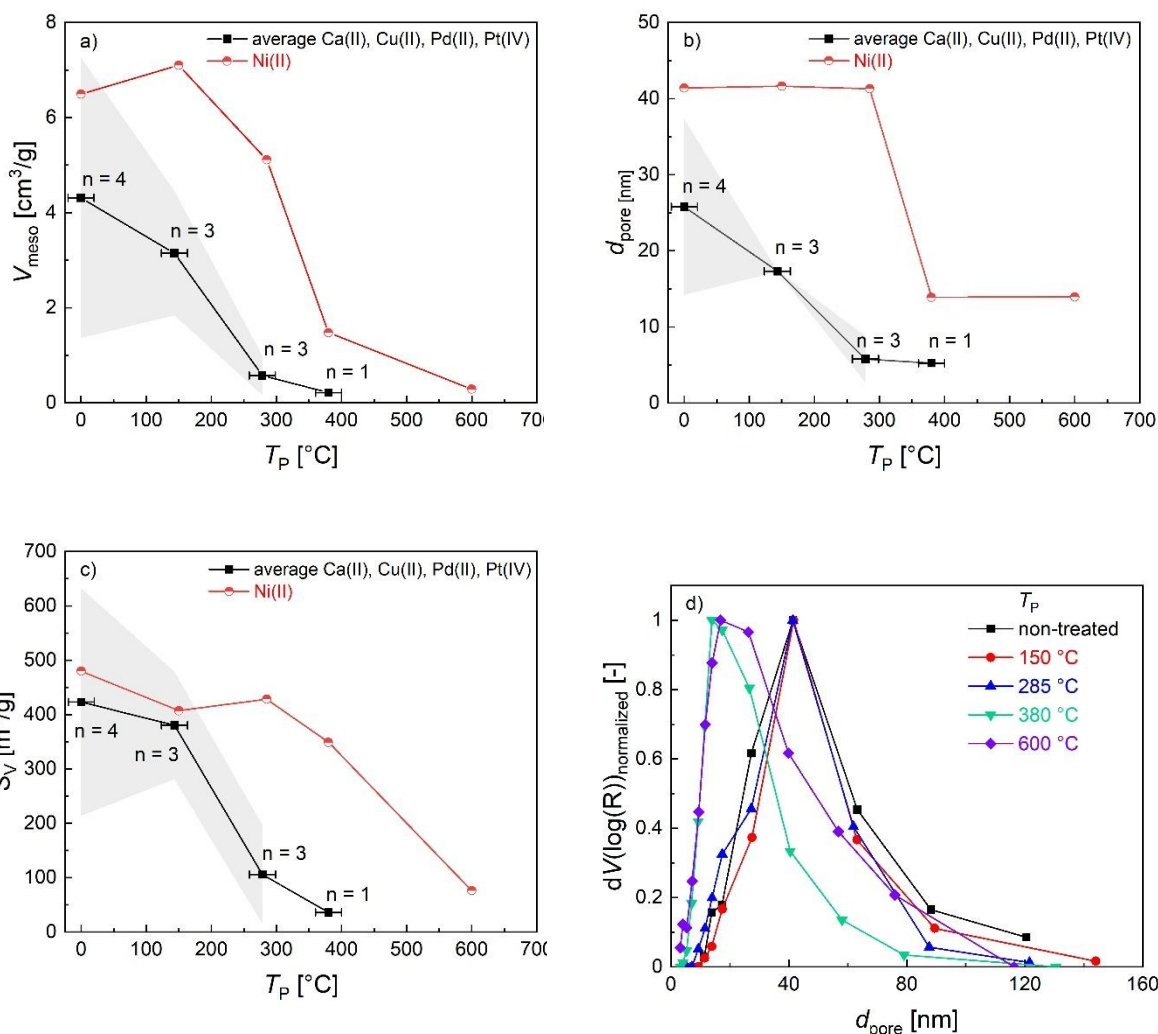
351 Because the degree of conversion α is normalized with respect to the final mass, samples with
352 significantly different metal/metal oxide content (such as Pd-CA and Pt-CA) can be directly compared.

353 It is notable that in the temperature range $T_P < 310$ °C the degree of conversion of Ni-CA is the lowest
354 curve compared to other M-CAs, while no further decomposition of Ni-CA took place at $T_P > 460$ °C.

355 Furthermore, the shape of the curves for Ca-, Cu and Pt-CAs is similar for high conversions ($\alpha >$
356 63 %) which are readily achieved in the low temperature range ($T_P < 270$ °C), followed by a slower

357 decomposition at higher conversions. Pd-CA shows both, a low T_{onset} as well as rapid decomposition
358 in the low temperature range.





359

360

361 **Fig. 3** Change of a) V_{meso} , b) d_{pore} and c) S_V in dependence of T_P . Squares represent the average values from
 362 aerogels crosslinked with different metal ions, excluding Ni(II). Lines are drawn to guide the eye, error areas
 363 represent the standard deviation from averaged values (y-error), n represents the number of single values taken
 364 into account varying at different temperatures, error bars represent the range of averaged values of T_P (x-error).
 365 Values at $T_P = 0$ $^{\circ}\text{C}$ represent non-pyrolysed M-CAs. d) Normalized pore size distributions of Ni-crosslinked gels
 366 heated up to different temperatures. Lines are drawn to guide the eye.

367 Since mass loss in aerogels pyrolysis is connected to textural properties, changes in the mesoporous
 368 structure during pyrolysis were followed via N_2 sorption analysis of samples, which were pyrolyzed
 369 up to four different T_P values whereas the pyrolysis process was stopped after the most significant
 370 mass loss steps respectively ($T_P = 130 - 150$ $^{\circ}\text{C}$, $265 - 285$ $^{\circ}\text{C}$, 380 $^{\circ}\text{C}$, 600 $^{\circ}\text{C}$). The general trend is
 371 that the S_V and V_{meso} values decrease over the course of the pyrolysis process (**Fig. 3, a – c**), with



372 the most significant changes being directly related to different steps of the mass loss. With the
373 exception of Ni(II)-crosslinked aerogels, pyrolysis up to $T_p = 285$ °C results in a significant loss of
374 mesoporosity. This is also reflected in the applicability of BET/BJH-methods: the M-CAs and materials
375 obtained at low pyrolysis temperatures show typical type IV-isotherms and highly correlated BET-
376 plots (**Fig. S12**, R^2 0.9991—0.9999), whereas determination of the textural properties via N_2 -
377 porosimetry is not possible for most M-DCs obtained at values of $T_p > 300$ °C. To date, the exact
378 mechanisms behind the transformation of the intrinsic biopolymer-aerogel pore structure to the
379 corresponding carbon network have not been revealed: due to the complexity of the pyrolysis
380 process, it seems reasonable to assume that different effects might dominate the transition depending
381 on the starting material and its intrinsic pore structure. From a fundamental point of view, the following
382 processes might lead to the diminishing, shrinkage, or formation of porous voids in the system, e.g.,
383 a) partial collapse of the already existing macro- and mesoporous network resulting from mass loss
384 in the form of gases. During this process, effects like pore-opening and pore-enclosure might occur
385 in different temperature ranges of the pyrolytic treatment.^[38] b) Creation of new pores by evaporation
386 of material from the bulk phase. In case of the latter, the existence of a pore network in the starting
387 material is not essential to obtain carbon aerogels, and pores could be formed by starting from a
388 multi-component system followed by pyrolysis or subsequent etching of only one component
389 (template-approach), as has e.g. been shown for polymer crosslinked silica-based xerogel
390 powders.^[39] In our case (one component system, if metal-ions are neglected), the mass loss during
391 pyrolysis may result in transformation of the already existing pores. This is reflected in the
392 mesoporous range by BJH-pore size distributions of Ni(II)-crosslinked gels: while no changes are
393 observed up to $T_p = 285$ °C, further increase to $T_p = 380$ °C results in a shift in the mesoporesize-
394 distribution to smaller pore sizes, being indicative for shrinkage of intrinsic mesopores (**Fig. 3, d**). It
395 is interesting to note that this effect coincides with the $T_{3_{max}}$ -signal in the corresponding DTG-curve
396 (**Fig. 2, b**), showing that prior mass-loss of up to 46% ($T_{2_{max}}$ -signal) did not lead to substantial
397 changes of the pore network. The additional increase in the pyrolysis temperature up to $T_p = 600$ °C
398 then leads only to small changes in the textural properties (a slight broadening of the pore size



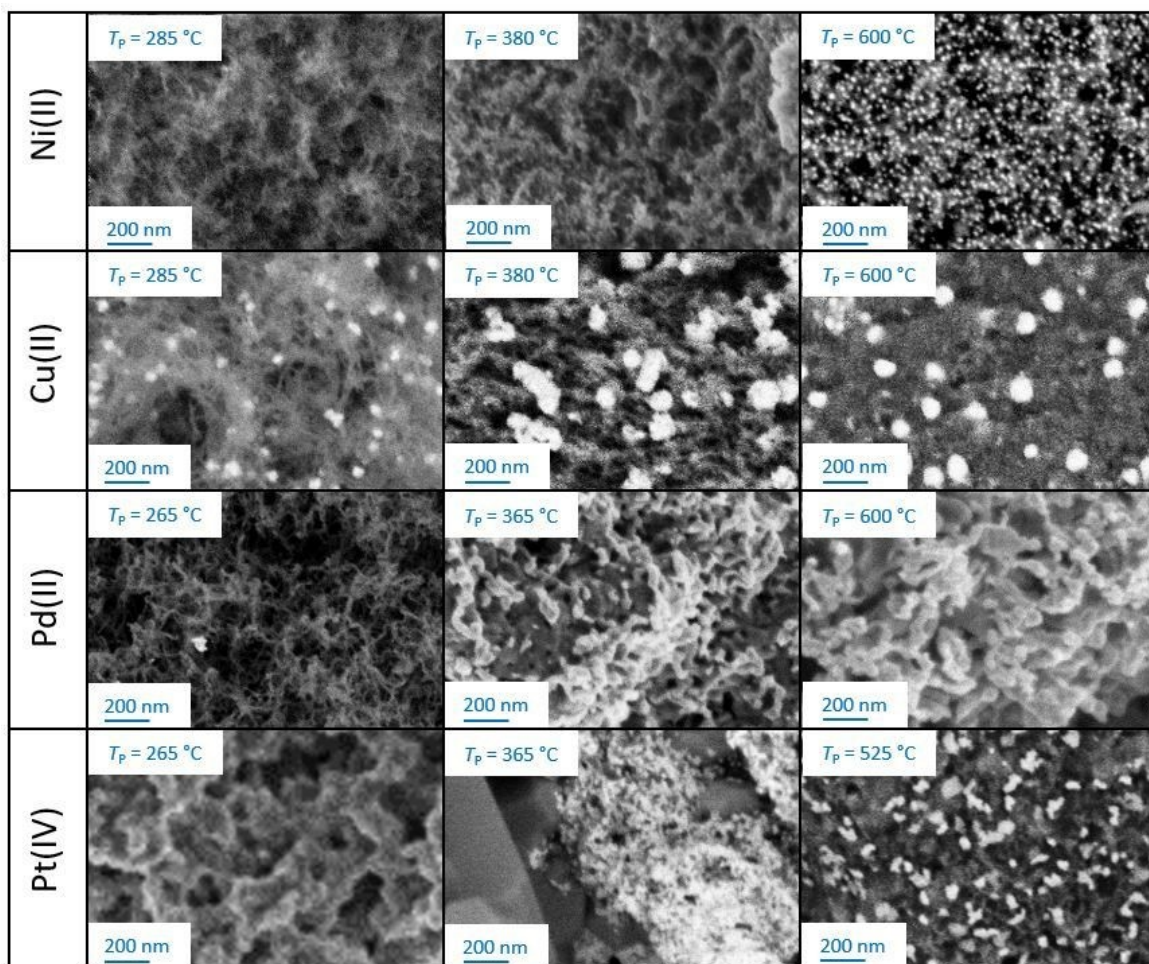
399 distribution and an increase in the pore volume in the range of larger mesopores), which is consistent
400 with the minor mass loss occurring in the temperature range between $T_p = 380 - 600$ °C (**Fig. 2, a,**
401 **b**). In summary, our results suggest that a slower and uniform conversion rate of organic material, as
402 obtained for Ni-CA, is beneficial for the (partial) preservation of mesoporosity.

403

404 *Influence of pyrolytic treatment on backbone morphology and evolution of nanoparticles*

405 Pyrolysis of M-CAs resulted in pronounced volumetric shrinkage of beads (approx. 31 - 52%),
406 whereas structural integrity was generally maintained (**Fig. S13**). However, in the case of Cu-DC and
407 Pd-DC, some morphological changes are visible in SEM pictures, which indicate fast shrinkage or
408 outgassing processes due to the comparably fast conversion in the lower temperature range (see
409 **Fig. 2d**). In contrast, no defects in Ca-DC and Ni-DC beads were identified. SEM-BSE data provide
410 a qualitative assessment of the morphological changes and especially the evolution of emerging
411 nanoparticles during pyrolysis: as the intensity of BSE strongly depends on the atomic number, metal-
412 containing structures are visible as brighter zones embedded in the darker biopolymer/carbon
413 backbone (**Fig. 4**).





414

415 **Fig. 4** Exemplary SEM-BSE images of M-DCs obtained after stopping the pyrolysis temperature at three different
 416 temperatures T_p .

417 Besides the evolution of the nanoparticles, changes of the backbone can also be observed: all
 418 materials obtained at $T_p = 285$ °C still show a fibrous structure that is typical for biopolymer aerogels
 419 (Pt-crosslinked aerogel represents an exception). At higher pyrolysis temperatures, the backbone
 420 demonstrates further densification and reduction in pore size. While all aerogels remain porous upon
 421 pyrolysis, the pore densification process during pyrolysis is highly influenced by the crosslinking
 422 metal. Optical evaluation of SEM-BSE pictures allows for a rough categorization: the best resistance
 423 against temperature-induced morphological changes is observed in the following order: Ni(II) > Cu(II)
 424 > Pd(II) > Pt(IV). This qualitative result highlights the crucial influence of crosslinking metals ion on
 425 the materials resulting from carbonization process.⁸ The result is also in line with BET/BJH and TGA



426 finding as well as with former work on Ni- and Cu crosslinked alginate.³³ In the following, trends in the
427 evolution of nanoparticles are described for each crosslinking ion. An overview of all results is
428 provided in **Table 3**.

429 **Table 3** Average particle size/species of metal NPs in different M-DCs determined via SEM-BSE and XRD.

M-DC	T_P (°C)	Species [-]	d_{NP} estimated via image analysis [nm]	Crystallite size estimated via XRD [nm]
Ni-DC	380	NiO	–	8 ± 1
Ni-DC	600	NiO	14 ± 7	23 ± 2
Cu-DC	285	Cu	40 ± 19	15 ± 5
Cu-DC		Cu ₂ O		23 ± 15
Cu-DC	600	Cu	85 ± 29	21
Cu-DC		CuO		25 ± 6
Pt-DC	525	Pt	33 ± 23	25 ± 5

430

431 *Ni-carbogels*

432 Below $T_P = 380$ °C no NPs are observed neither in BSE-SEM nor in XRD. After pyrolyzing the
433 aerogels up to $T_P = 380$ °C, the BSE image shows tiny, well-defined NPs (**Fig. 4**); however,
434 determination of the NP size is not possible due to low contrast. Bragg's peaks of nickel(II)-oxide
435 (NiO) were detected by XRD (**Fig. 5, a**) with an average crystallite size of approximately 8 ± 1 nm.
436 Pyrolysis at $T_P = 600$ °C also results in the formation of NiO-NPs. The average NP size is determined
437 to be 14 ± 7 nm from the BSE images (**Fig. 4**), whereas significantly larger crystallite sizes of NiO
438 NPs of (23 ± 2 nm) were detected based on narrow NiO Bragg peaks (**Fig. 5, a**). The diffraction peaks
439 at 44.52 , 51.83 and 76.34° are indicative of the face-centered cubic (fcc) phase of crystalline Ni
440 (JCPDS no. 04–0850) corresponding to (111), (200), and (220) planes of crystalline elementary Ni.⁴¹
441 At a pyrolysis temperature of $T_P = 600$ °C, these peaks become more detached from the NiO peak.
442 NiO peaks are still present but weaker than at $T_P = 380$ °C. This decrease in intensity can be attributed
443 to the growth of crystallite size in both NiO and Ni, resulting in narrower peaks in the XRD pattern.
444 Rietveld analysis was used to estimate the composition of Ni and NiO. It was shown that the amount



445 of Ni significantly decreased during high-temperature pyrolysis, i.e. the ratio of NiO and Ni was
446 90.4% : 9.6% at 380 °C vs. 95.4% Ni : 4.6% at 600 °C. The temperature increase can lead to the
447 sintering of metallic nickel into larger crystallites of metal, driven by the transformation of different
448 crystal forms (e.g., 111, 200, 220) of nickel..⁴²

449

450 *Cu-carbogels*

451 Cu containing aerogels pyrolyzed at different temperatures lead to the formation of NPs of different
452 chemical compositions at lower pyrolysis temperatures than for Ni-CA. Bragg's peaks of elementary
453 copper and copper (I) oxide were observed in samples pyrolyzed up to $T_p = 285$ °C, however, copper
454 (II) oxide dominates (with only traces of elementary copper detected) in the NPs after pyrolysis up to
455 $T_p = 600$ °C (**Fig. 5, b**). Pyrolysis of Cu-CA under comparable conditions resulted in metallic Cu and
456 Cu₂O crystallites, as a result of the redox reaction between Cu(II) and sugars, suggesting that during
457 pyrolysis a carbothermal reduction of the metal ion occurred.⁸ In the work by Baumann *et al.*, metal
458 particles with no sign of metal-oxides in the XRD patterns were formed upon pyrolysis of resorcinol-
459 formaldehyde aerogels containing M(II) cations (Ni, Co, Cu).¹¹ The reason for the complete reduction
460 in this case, and only partial reduction of the present work, can be that the resorcinol-formaldehyde
461 resin is a reductive matrix, while the alginate is not necessarily. Besides oxidative state, the size of
462 Cu-NPs also changed over the course of the pyrolysis: analysis of BSE images obtained at
463 $T_p = 285$ °C shows that the particle size of Cu/Cu₂O NPs is 40±20 nm (**Fig. 4**), while the size of
464 CuO/Cu NPs obtained at $T_p = 380$ and 600 °C is significantly larger as compared to NiO NPs: 85 ±
465 29 nm. The average crystallite size for each component of the NPs was calculated from the XRD
466 data. A significant discrepancy can be seen between XRD and BSE data for the particle size. The
467 reason is that the XRD can estimate the crystallite size of the NPs and not the physical size of the
468 NPs. The general trend that the crystallite size increases with increasing pyrolyzing temperature holds
469 true for all components (see **Table 3**). According to the result of the Rietveld analysis, we found the
470 following: the ratio of elementary Cu and Cu₂O is 51.6% and 48.4% in the case of low-temperature



471 pyrolysis, however, a significantly lower amount of Cu(0) has been detected after high-temperature
472 pyrolysis, with a 0.7% Cu to 99.3 % CuO ratio.

473

474 *Pd-carbogels*

475 In the case of Pd-DC, no formation of defined nanoparticles was observed via SEM-BSE. Brighter
476 zones of samples produced at $T_P \geq 365$ °C indicate the formation of Pd-layers around the carbon
477 backbone, most probably due to the high final metal content (**Fig. 4**). XRD data show that the metal
478 part of the sample is in a crystalline state after pyrolyzing at $T_P = 265$ °C, i.e. that 63.4% Pd and
479 36.6% PdO can be estimated by the Rietveld analysis (**Fig. 5, c**). This ratio changed slightly for the
480 samples pyrolyzed at $T_P = 600$ °C, resulting in a ratio of 46.9% Pd and 53.1% PdO.

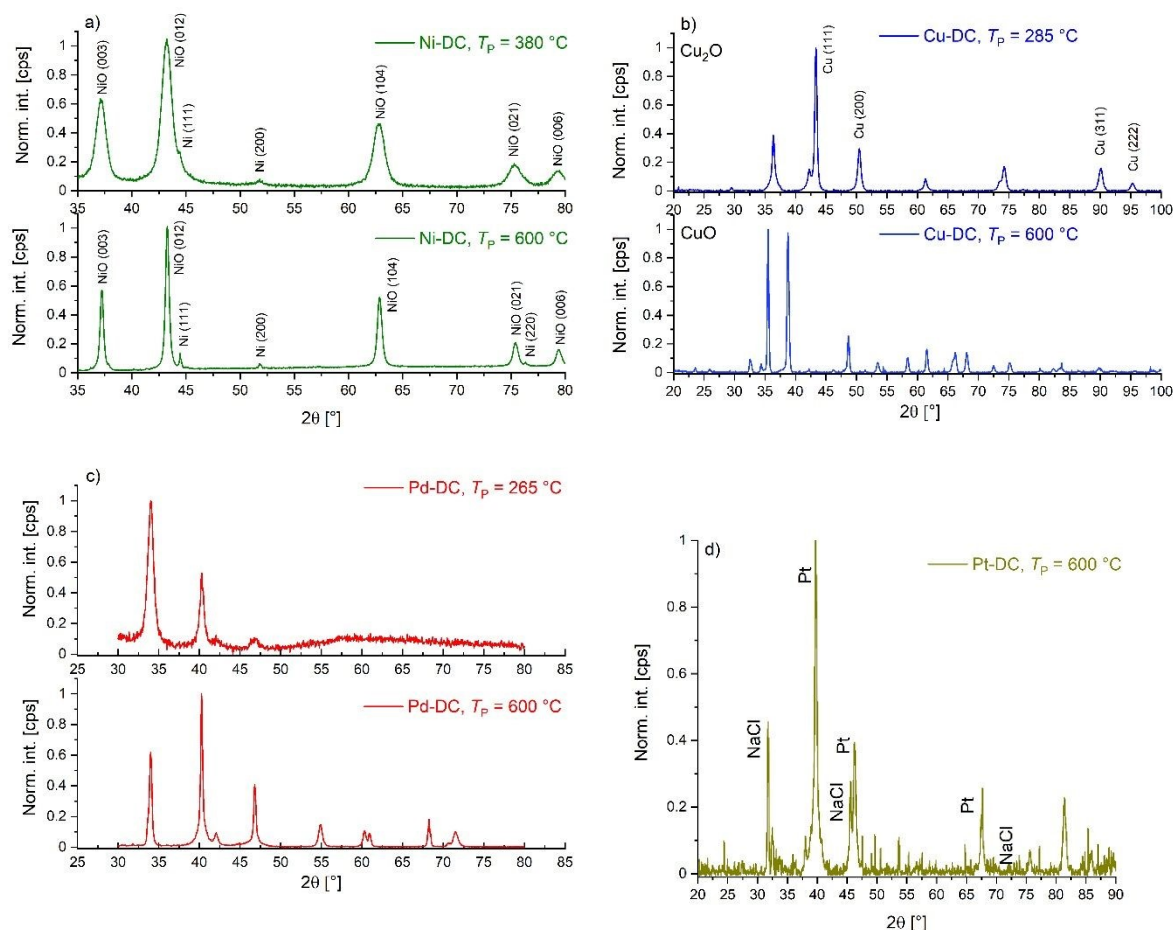
481

482 *Pt-carbogels*

483 NPs could be detected in the carbogel only after pyrolyzing at 525 °C. However, the shape of the NPs
484 is not well-defined compared to those of the Ni- and Cu-carbogels. The BSE image of the Pt-carbogel
485 sample clearly shows (**Fig. 4**) the appearance of large, irregular shaped NPs. XRD measurements
486 also confirmed that elementary Pt is the dominant component of the NPs (**Fig. 5, d**). Additionally,
487 Bragg's peaks of sodium chloride were also detected, which was expected due to its low solubility in
488 ethanol in the solvent exchange step and therefore reaction of Na-ions from sodium alginate and
489 chlorine from PtCl₄ during pyrolysis. The size of Pt-NPs is 33 ± 23 nm according to the image analysis
490 of BSE pictures and in agreement with the evaluation of the XRD data (**Table 3**).

491





492

493

494

495

Fig. 5 XRD patterns of different metallic metal/metal oxide nanoparticles obtained from different M-Cas and different values of T_p : a) Ni-DC, b) Cu-DC, c) Pd-DC, d) Pt-DC.

496

Reducibility of metal oxides

497

498

499

500

501

502

503

504

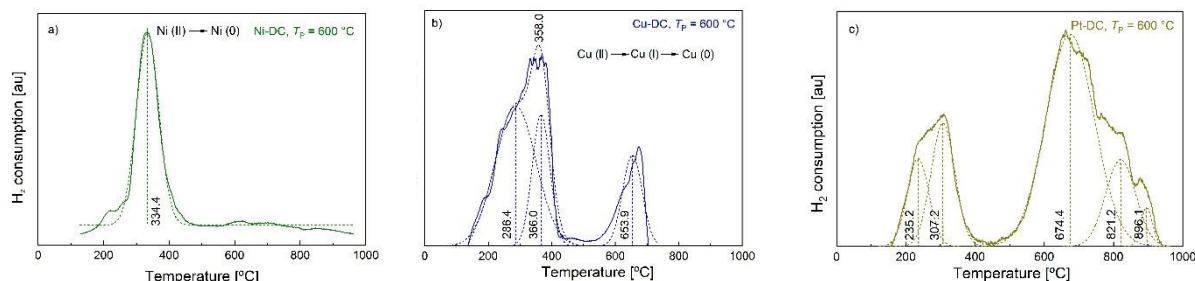
505

The temperature programmed reduction (TPR) technique allows determining the reduction temperature of metal oxides, revealing its reducibility, which is an important parameter to determine the optimal activation conditions for potential applications.⁴³ H₂-TPR of Ni-DC ($T_p = 600\text{ °C}$) (Fig. 6) showed a main broad peak at 334.3 °C, characteristic of the reduction region of Ni(II) to Ni(0) (378 °C for bulk NiO, and 382 °C for a Ni4.3%/AC catalyst), confirming that there is only one oxidative state in Ni-DC.^{44,45} The slightly lower reduction temperature (334.3 °C) may be related to the higher metal content in the Ni-DC (9.5%), also reflected by the broad shape of the reduction peak, thus providing a weak surface level interaction between Ni and hydrogen. This higher reducibility is comparatively competitive to other Ni based catalysts with similar metal content and lower reducibility, such as



506 Ni10%/AC (main peak at 430 °C).⁴⁶ This imply an easier activation pretreatment of Ni-DC would be
 507 needed in further applications. Moreover, the Ni-DC did not present significant gasification of the
 508 carbon lattice, that usually onsets from 600 °C for carbon supports, hence supporting evidence of its
 509 thermal stability.^{47,48}

510 **Fig. 6** also illustrates the reduction of copper at different oxidative states, observing two major steps.
 511 The first one starts developing from 60 °C and is completely completed at 420 °C, corresponding to
 512 the reduction of CuO species (Cu(II)) to Cu₂O (Cu(I)) and Cu(0).⁴⁶ The second one onsets at 520 °C,
 513 with a maximum at 673 °C. Since copper oxide species completely reduce to metallic Cu(0) at
 514 temperatures no further than 420 °C, this second step should be explained by the gasification of the
 515 carbon backbone of the Cu-DC sample.^{49,50}



521

522 **Fig. 6** H₂-TPR curves of M-DCs produced at $T_P = 600$ °C. Straight lines represent raw data, dashed lines the
 523 deconvoluted peaks and according maxima.

524 The deconvoluted reduction peaks of Pt-DC at 235.2 and 307.2 °C (**Fig. 6 c**) can be attributed to the
 525 reduction of bulk and inter surficial PtO_xCl_y, as suggested by Hwang et al., originating from traces of
 526 the PtCl₄ precursor.⁵¹ Furthermore, HCl desorption has also been identified within this temperature
 527 range.⁵² It appears that there is an absence of typical PtO_x reduction peaks (expected to be below
 528 200 °C),⁵³ probably associated with the poor crosslinking that displayed the Pt-CA. This means that
 529 unlike Ni, Cu and Pd, Pt does not catalyze the oxide formation during carbonization. Finally,
 530 gasification of the Pt-DC sample is observed from 450 to 950 °C. The TPR curves of Pd-DC where
 531 not possible to obtain with the method used, in order to avoid serious damage on the chemisorption
 532 equipment, due to the detection of condensable substances. In summary, H₂-TPR analysis shows



533 that among the tested M-DCs, Ni-DC has the best performance toward activation by the H₂ reduction
534 process, because it presents: i) only one single reduction step, ii) the lowest reduction temperature,
535 iii) the highest thermal stability of the carbon backbone as indicated by a minimal gasification.

536

537 **CONCLUSIONS**

538

539 This work presents a facile method for the production of nanoparticle-decorated porous carbons by
540 pyrolysis of aerogels obtained via crosslinking of sodium alginate with different metal ions and
541 supercritical drying. The broad variety of textural properties obtained for parent aerogels emphasizes,
542 that choice of crosslinking metal ions is a suitable tool for manipulating the pore structure in alginate
543 aerogel synthesis. In the pyrolysis step up to 600 °C, all M-DCs showed a significant mass loss and
544 loss a of mesoporosity, whereas the highest stability was identified for the Ni-crosslinked gel with the
545 lowest conversion rate during pyrolysis, which shows the significant influence of the metal ion used
546 on the pyrolysis mechanism. XRD and BSE measurements show the growth of metal(oxide)
547 nanoparticles from the intrinsically molecularly distributed metal ions and the possibility of generating
548 a carbon matrix with homogeneously distributed NPs. While the advantages of this approach lie
549 clearly in its green nature and the avoidance of costly and time consuming post-processing steps (like
550 e.g. wet-impregnation our supercritical deposition) in order to distribute NPs in the carbon matrix, it
551 has to be pointed out, that limitations are given by the fact, that the properties of nanoparticles and
552 porous matrix cannot be changed independently. In order to achieve desired nanoparticle sizes with
553 metals of choice, individual strategies have to be developed which could include the use of
554 crosslinking metal ion mixtures, variation of alginate and metal-precursor concentrations and the use
555 of alginates with different M- to G-ratios. Compared to the properties of conventional carbogels based
556 on resorcinol-formaldehyde, the M-DCs developed in this work showed significantly lower specific
557 surface area and higher mass loss during pyrolysis.^[54] The optimization potential becomes evident
558 when considering that the pyrolysis temperatures employed in this study remain below the threshold
559 at which micropore formation might occur. Hence, the application of a higher $T_p \geq 800$ °C is a



560 promising next step, which is expected to result in the formation of additional micropores. Enhanced
561 preservation of the mesopore volume/specific surface area may be achieved by employing lower
562 heating rates during pyrolysis (e.g., in the range of 1.0 – 2.5 °C/min), as has already been reported^[39]
563 and is also indicated by our results with the lowest conversion rate yielding comparably best textural
564 features of the carbon matrix. A further possibility to reduce mass loss and to improve textural
565 properties is the introduction of lignins or tannins into the alginate matrix as both biopolymers have
566 reactivity and properties similar to those of resorcinol and phenol and have already successfully been
567 used as non-toxic replacement with natural origin.^[55] We believe that studies conducted in this work
568 are helpful in identifying suitable conditions and might therefore contribute to the development of
569 catalyst-systems based on green synthesis routes.

570

571 **Author contributions**

572 Juan I. del Río: investigation, original draft, formal analysis. Laura Juhász: investigation, formal
573 analysis. József Kalmár: conceptualization, formal analysis, editing. Zoltán Erdélyi: investigation.
574 María D. Bermejo: investigation. Ángel Martín: investigation. Irina Smirnova: resources. Pavel
575 Gurikov: project administration, formal analysis, editing, Baldur Schroeter: conceptualization, original
576 draft, formal analysis.

577 **Conflicts of interest**

578 There are no conflicts to declare.

579 **Acknowledgements**

580 This project has been funded by the Ministry of Science and Universities through project RTI2018-
581 097456-B-I00 and by the Junta de Castilla y León through project by FEDER FUNDS under the
582 BioEcoUVa Strategic Program (CLU-2019-04).

583

584 Juan Ignacio del Río acknowledges Universidad de Valladolid for the predoctoral and postdoctoral
585 fellowships, as well as to the programs i) MOVILIDAD DOCTORANDOS Y DOCTORANDAS UVa
586 2021, and ii) PRÁCTICAS ERASMUS EN EMPRESAS EXTRANJERAS CON SEDE EN EL



587 ESPACIO EUROPEO DE EDUCACIÓN SUPERIOR (EEES) Y PAISES ASOCIADOS DEL
588 PROGRAMA.

589 The XRD and the SEM measurements were financially supported by the TKP2021-NKTA-34 project
590 implemented with the support provided from the National Research, Development and Innovation
591 Fund of Hungary, financed under the TKP2021-NKTA funding scheme.

592

593

594



595 REFERENCES

- 596 1 S. S. Kistler, *Nature*, 1931, **127**, 741.
- 597 2 S. S. Kistler, *Rubber Chem. Technol.*, 1932, **5**, 600–603.
- 598 3 A. C. Pierre and G. M. Pajonk, *Chem. Rev.*, 2002, **102**, 4243–4266.
- 599 4 C. Moreno-Castilla and F. J. Maldonado-Hódar, *Carbon*, 2005, **43**, 455–465.
- 600 5 R. W. Pekala, *J. Mater. Sci.*, 1989, **24**, 3221–3227.
- 601 6 J.-H. Lee and S.-J. Park, *Carbon*, 2020, **163**, 1–18.
- 602 7 P. Paraskevopoulou, D. Chriti, G. Raptopoulos, and G. C. Anyfantis, *Materials*, 2019, **12**,
603 1543.
- 604 8 G. Raptopoulos et al., *Mater. Adv.*, 2021, **2**, 2684–2699.
- 605 9 Y. Zhang et al., *Adv. Funct. Mater.*, 2021, **31**, 2104377.
- 606 10 T. F. Baumann, G. A. Fox, J. H. Satcher, N. Yoshizawa, R. Fu, and M. S. Dresselhaus,
607 *Langmuir*, 2002, **18**, 7073–7076.
- 608 11 T. F. Baumann and J. H. Satcher, *Chem. Mater.*, 2003, **15**, 3745–3747.
- 609 12 R. Luque, V. Budarin, J. H. Clark, and D. J. Macquarrie, *Appl. Catal. B Environ.*, 2008, **82**,
610 157–162.
- 611 13 B. A. T. Mehrabadi, S. Eskandari, U. Khan, R. D. White, and J. R. Regalbuto, *Adv. Catal.*,
612 2017, **61**, 1–35.
- 613 14 O. K. Lee and E. Y. Lee, *Biomass and Bioenergy*, 2016, **92**, 70–75.
- 614 15 R. J. White, N. Brun, V. L. Budarin, J. H. Clark, and M. Titirici, *ChemSusChem*, 2014, **7**,
615 670–689.
- 616 16 L. Pereira and J. Cotas, in *Alginates: Recent Uses of This Natural Polymer*, ed. L. Pereira,
617 Intechopen, London, 1st edn, 2020, vol. 7, 1–150.
- 618 17 E. M. Ahmed, *J. Adv. Res.*, 2015, **6**, 105–121.
- 619 18 X. Meng, X. Tian, Y. Xia, and Z. Xiong, *J. Dispers. Sci. Technol.*, 2021, **43**, 1–8.
- 620 19 S.-M. Alatalo et al., *ACS Appl. Mater. Interfaces*, 2015, **b**, 25875–25883.
- 621 20 reduction.



- 622 21 B. Schroeter et al., *Cellulose*, 2021, **28**, 223–239.
- 623 22 L. E. Flint and A. L. Flint, in *Methods of Soil Analysis: Part 4 Physical Methods*, ed. J. H. Dane and G. C. Topp, Soil Science Society of America, Madison, 2002, 241–254.
- 624
- 625 23 L. Juhász et al., *Polymers (Basel)*, 2021, **13**, 588.
- 626 24 R. P. Narayanan, G. Melman, N. J. Letourneau, N. L. Mendelson, and A. Melman,
- 627 *Biomacromolecules*, 2012, **13**, 2465–2471.
- 628 25 C. Richardson-Boedler, *Toxicol. Environ. Chem.*, 2007, **89**, 15–70.
- 629 26 C. Hu, W. Lu, A. Mata, K. Nishinari, and Y. Fang, *Macromolecules*, 2021, **177**, 578–588.
- 630 27 S. P. Raman et al., *J. Supercrit. Fluids*, 2019, **153**, 104545.
- 631 28 C. Keil et al., *Polymers (Basel)*, 2020, **12**, 1–17.
- 632 29 J. M. Miller and B. Dunn, *Langmuir*, 1999, **15**, 799–806.
- 633 30 S. M. Alay-e-Abbas, K. Mahmood, A. Ali, M. I. Arshad, N. Amin, and M. S. Hasan, in *Micro and Nano Technologies, Bionanocomposites*, ed. K. M. Zia, F. Jabeen, M. N. Anjum, S. Ikram, Elsevier, 2020, ch. 5, 105–144.
- 634
- 635
- 636 31 J. S. Rowbotham, P. W. Dyer, H. C. Greenwell, D. Selby, and M. K. Theodorou, *Interface Focus*, 2013, **3**, 20120046.
- 637
- 638 32 M. J. Zohuriaan and F. Shokrolahi, *Polym. Test.*, 2004, **23**, 575–579.
- 639 33 Y. Liu et al., *RSC Adv.*, 2015, **5**, 64125–64137.
- 640 34 E. Widjaja, H. H. Chong, and M. Tjahjono, *J. Raman Spectrosc.*, 2010, **41**, 181–186.
- 641 35 R. L. White, *Thermochim. Acta*, 2012, **528**, 58–62.
- 642 36 W. Brockner, C. Ehrhardt, and M. Gjikaj, *Thermochim. Acta*, 2007, **456**, 64–68.
- 643 37 A. Alba, M. A. Aramendia, V. Borau, C. Jimenez, and J. M. Marinas, *J. Catal.*, 1986, **98**,
- 644 288–295.
- 645 38 S. Seleem, M. Hopkins, J. Olivio, and D. A. Schiraldi, *Ohio J. Sci.*, 2017, **117**, 50–60.
- 646 39 M. A. T. Jaya, W. M. H. F.W. Harun and M. A. Ahmad, *Journal of Applied Sciences*, 2014,
- 647 **14**, 1359–1364.
- 648 40 R. U. Soni et al., *Chem. Mater*, 2022, **34**, 4828–4847.



- 649 41 C. Teng et al., *Nanoscale Res. Lett.*, 2015, **10**, 384.
650
- 651 42 E. D. Garbowski, C. Mirodatos, and M. Primet, in *Studies in Surface Science and Catalysis*,
652 Elsevier, 1982, 235–243.
- 653 43 M. A. Reiche, M. Maciejewski, and A. Baiker, *Catal. Today*, 2000, **56**, 347–355.
654 44 A. Alihosseinzadeh, B. Nematollahi, M. Rezaei, and E. N. Lay, *Int. J. Hydrogen Energy*, 2015,
655 **40** 1809–1819.
- 656 45 Q. Zeng et al., *Environ. Sci. Pollut. Res.*, 2019, **26**, 15420–15435, 2019.
657 46 R. Merabti, K. Bachari, D. Halliche, Z. Rassoul, and A. Saadi, *React. Kinet. Mech. Catal.*,
658 2010, **101**, 195–208.
- 659 47 M. Trépanier, A. Tavasoli, A. K. Dalai, and N. Abatzoglou, *Appl. Catal. A Gen.*, 2009, **353**,
660 193–202.
- 661 48 G. Zhang, Z. Li, H. Zheng, T. Fu, Y. Ju, and Y. Wang, *Appl. Catal. B Environ.*, 2015, **179**,
662 95–105.
- 663 49 G. Fierro, M. Lojacono, M. Inversi, P. Porta, R. Lavecchia, and F. Cioci, *J. Catal.*, 1994, **148**,
664 709–721.
- 665 50 K. Sonobe, M. Tanabe, T. Imaoka, W. Chun, and K. Yamamoto, *Chem. Eur. J.*, 2021, **27**,
666 8452–8456.
- 667 51 C.-P. Hwang and C.-T. Yeh, *J. Mol. Catal. A Chem.*, 1996, **112**, 295–302.
668 52 M. A. Fraga, E. Jordao, M. J. Mendes, M. M. A. Freitas, J. L. Faria, and J. L. Figueiredo, *J.*
669 *Catal.*, 2002, **209**, 355–364.
- 670 53 T. Huizinga, J. Van Grondelle, and R. Prins, *Appl. Catal.*, 1984, **10**, 199–213.
671 54 F. Li et al., *Microporous and Mesoporous Materials*, 2019, **279**, 293–315.
672 55 D. K. Sam et al., *Carbohydrate Research*, 2020, **491**, 107986.
673
674

